Materials and Design 176 (2019) 107836

Contents lists available at ScienceDirect

Materials and Design

journal homepage: www.elsevier.com/locate/matdes

The effect of the size of NbTi filaments on interfacial reactions and the properties of InSn-based superconducting solder joints

S. Santra *, T. Davies, G. Matthews, J. Liu, C.R.M. Grovenor, S.C. Speller

Department of Materials, University of Oxford, OX1 3PH, UK

HIGHLIGHTS

- Interaction of NbTi with InSn produces an intermetallic phase, (Nb,Ti)Sn_2, with randomly crystallographic oriented grains.
- Larger filaments form thin uniform (Nb,Ti)Sn_2 phase with negligible Ti-solubility.
- Large (Nb,Ti)Sn_2 scallops grow with significant Ti-concentration for finer filaments.
- Irreversibility field and flux line pinning force of NbTi changes owing to coarsening of α-Ti precipitates after soldering.
- No detectable interaction zone for NbTi–(In,Bi)Sn due to decrease in thermodynamic activity of Sn with addition of Bi.
- The property of bulk solder is regarded the limiting factor and not any interfacial reactions.

GRAPHICAL ABSTRACT

Elemental maps of the interaction zones developed in mono- and multi-filamentary NbTi–InSn solder reacted at 350 °C depicting the differences in chemical composition and morphology of the interfacial phase layers, and schematic illustration of development of these zones.

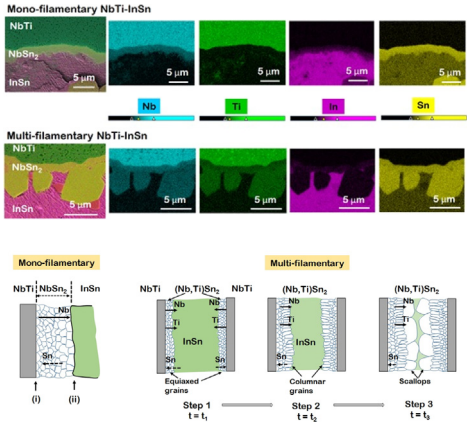

ARTICLE INFO

Article history:
Received 19 February 2019
Received in revised form 2 May 2019
Accepted 6 May 2019
Available online 9 May 2019

Keywords:
Diffusion
Microstructure
Flux-pinning
Soldering
Texture

ABSTRACT

Interactions of superconducting Nb(47 wt% Ti) with liquid binary In-35 wt% Sn and Bi-containing ternary (In, 15 wt% Bi)-35 wt% Sn solders have been examined for the first time up to 450 °C. Reaction of NbTi with InSn results in an intermetallic phase, (Nb,Ti)Sn_2, the morphology and chemical composition of which depends on the size of NbTi filaments. Larger filaments react to form a thin uniform (Nb,Ti)Sn_2 phase with a Nb:Ti ratio of 6:1, while for finer filaments large (Nb,Ti)Sn_2 grains grow with a Nb:Ti ratio of 0.5:1. Differences for interfacial phase layers have been explained by a diffusion-controlled growth model based on metallurgical state of NbTi filaments. Neither filamentary types exhibit any change in critical temperature (~9.2 K) after soldering treatment at 350 °C, but the irreversibility field and flux line pinning force of NbTi changes by a higher factor for the larger filaments. Interaction of NbTi with ternary (In,Bi)Sn results in a lack of any detectable interaction zone, and characteristic nucleation behaviour of phases in the bulk solder at NbTi–(In,Bi)Sn interface is rationalized on the basis of thermodynamic arguments. Transport measurements suggest that properties of solder are the limiting factor for joint behaviour and not any interfacial reactions.

* Corresponding author.
E-mail address: sangeeta.santra@gmail.com (S. Santra).

https://doi.org/10.1016/j.matdes.2019.107836

1. Introduction

The metallic low-temperature superconductor (LTS) alloy NbTi is an integral constituent of high-field superconducting magnets which find extensive applications in the medical sector (MRI), particle accelerators (Large Hadron Collider (LHC)) and large engineering research projects (poloidal field coils in ITER) owing to their reliable properties when manufactured as long wires. Large magnets consist of many individual LTS wires wound together forming a long solenoid, and for applications such as MRI must operate in a persistent mode with a closed superconducting circuit for uninterrupted current flow [1]. The assembly usually involves several soldered joints to connect shorter lengths of LTS wires, and these superconducting joints must have a resistance below ~10^{-13} Ω in magnetic fields typically ~1 T as well as having adequate mechanical strength [2]. Violation of either requirement may result in high thermal and magnetic flux dissipation, and a significant loss of magnet performance.

The current joining component for ductile NbTi superconducting wires is lead-based $Pb_{60}Bi_{40}$ (wt%) solder because of its low-melting point (120 °C), good wetting performance, prolonged fatigue life and demonstrated potential to manufacture reliable joints that carry persistent currents up to 1000 A at 4.2 K in a magnetic field of 1 T [2,3]. However, due to the adverse effects of lead on health and the environment, new European legislation forces the replacement of the current PbBi solder with a lead-free alternative in the magnet and electronic packaging systems [4]. Although several types of environmental-friendly Sn-based solders are widely used in the circuit packaging technology [5–8], no lead-free superconducting solder is in use for the practical applications so far. Among the many potent solder systems, recently binary $In_{65}Sn_{35}$ solder consisting of a matrix of In-rich β (In_3Sn) containing the Sn-rich γ-phase ($InSn_4$) and ternary $In_{50}Sn_{35}Bi_{15}$ (in wt%) solder, which is a three-phase mixture of β, γ and $BiIn_2$, have been explored as potential replacement materials [9]. Lead-free solders for high temperature superconducting soldered joints have also been explored by comparing joints fabricated between rare-earth-$Ba_2Cu_3O_7$ (REBCO) tapes using $In_{52}Sn_{48}$ with those made with $Pb_{38}Sn_{62}$ solders [10]. However, no study has been reported on lead-free superconducting solder joints for NbTi wires. The properties of a superconducting solder joint can be adversely affected by local variations in microstructure and by the composition of any interaction zone created between the solder and NbTi filaments by local diffusional processes during soldering operations. To be able to design optimum lead-free solder joints, it is important to understand the evolution of microstructure at the interface between NbTi filaments and InSn based solders and to understand the kinetics and thermodynamics of phase formation.

Magnet manufacturers use NbTi wires containing differently sized filaments depending on the specific local application; for example liquid helium level sensors use mono-filamentary NbTi, while multi-filamentary wires are designed for use in magnets for NMR, MRI and accelerators that require higher stability [11,12]. Hence, we have also studied the role of the initial metallurgical state of the NbTi filament on microstructural and microtexture evolution at the interface between solid NbTi and liquid InSn based solders. NbTi wires of two technologically relevant architectures, i.e. mono- and multi-filamentary, were procured from the same manufacturer. The diameter of the mono-filamentary NbTi is 250 μm, while the multi-filamentary wire consists of 54 single filaments each having a cross-sectional diameter of 45 μm, both within a copper matrix. The aim of this study is two-fold; firstly to examine the interaction behaviour of NbTi in contact with the liquid InSn based binary $In_{65}Sn_{35}$ and Bi-containing ternary $(In_{50}Bi_{15})Sn_{35}$ solders in the soldering temperature range of 250 to 450 °C, and second to study any changes induced in the superconducting properties of two different filamentary types of NbTi as a result of soldering. Unusually long interaction times up to 361 h have been chosen to show more clearly the underlying growth mechanism in the interaction zone, and to correlate these with the relevant superconducting properties.

2. Experimental methods

2.1. Soldering

Two solders, binary $In_{65}Sn_{35}$ ($In_{65.8}Sn_{34.2}$ at.%) called InSn and ternary $(In_{50}Bi_{15})Sn_{35}$ ($In_{54.3}Sn_{36.8}Bi_{8.9}$ at.%) called (In,Bi)Sn, were prepared by melting pure Sn (99.995 wt%), In (99.999 wt%) and Bi (99.95 wt%) in a silica crucible at 350 °C on a hot-plate, followed by gentle stirring for better homogeneity and poured into a copper mould. The mono- and multi-filamentary NbTi wires with copper stabilizer were procured from Supercon Inc., and in order to expose the NbTi filaments and avoid surface oxidation, the wires were dipped in a molten tin bath at 350 °C for 10 min. The procedure follows the steps of Thornton's matrix replacement soldering technique for NbTi [13]. The thickness of the copper coating was 75 μm for the monofilament ($area_{Cu}$: $area_{NbTi}$ = 1.5), while the $area_{Cu}$: $area_{NbTi}$ was 1.3 for the multi-filamentary wire. The isothermal interactions of NbTi filaments with the solders were conducted in a calibrated box furnace in air at temperatures ranging from 250 to 450 °C (±5 °C) for times as long as 361 h. The solder-reacted NbTi filaments were cross-sectioned, mounted in a steel clip and embedded in cold mounting resin because of the low-melting temperatures of the InSn (~140 °C) and (In,Bi)Sn (~50 °C) solders, and polished using conventional metallographic techniques followed by fine polishing with colloidal silica and coated with carbon for microstructural analysis.

2.2. Microstructural and texture characterization

Phase and microstructural evolution at the NbTi–solder interface was studied in a field-emission scanning electron microscope (FE-SEM) equipped with an energy dispersive X-ray (EDX) detector operated at 10 kV and 500 pA to perform high resolution composition analysis. The micro-texture evolution in the interaction zone was examined using electron back-scattered diffraction (EBSD). Thin lift-out lamellae of approximately 45 nm thickness were prepared from the transverse cross-section of the two differently sized NbTi filaments by focussed ion beam (FIB) milling to study nanometre scale microstructural features by transmission electron microscopy (TEM) at 300 keV and transmission Kikuchi diffraction (TKD). Accelerating voltages of 20 kV and 30 kV, beam current of 15 nA and 2 nA, and step size of 50 nm and 4 nm were used during data acquisition for conventional EBSD and TKD respectively. A Bruker EBSD camera coupled with Esprit software was used for data acquisition, and the post-processing was conducted using HKL software. Clean up procedure was carried out up to a limit of 0.1. Grain tolerance angle of 5° was chosen to define the locations of grain boundaries in both these cases. The black pixels in all the orientation maps denote the unsolved patterns, and the black lines are the grain boundaries.

2.3. Superconducting-property and critical current measurements

Superconducting properties were measured in a 16 T Quantum Design Physical Properties Measurement System (PPMS) with vibrating sample magnetometer (VSM) option. Cylindrical samples were cut to a fixed length of 3.1 mm to minimise any geometric effects, then fixed onto a quartz paddle using GE-varnish with the wire axis carefully aligned with the applied field. Critical temperature values (T_c) were determined from moment-temperature (M–T) sweeps acquired in the zero-field cooled regime at fields between 1 and 100 mT. Moment-applied field (M–H) curves were taken at 4.2 K with a sweep rate of 5 mT/s. Critical current densities (J_c) were calculated from these M–H curves using Bean's formula for a cylindrical sample [14].

Transport measurements to determine the critical current values of soldered NbTi joints were performed in liquid helium at 4.2 K in a Cryogenic Ltd. cryostat with 14 T magnet. The soldered joint was made using Thornton's matrix replacement method as explained above [13]. 15 mm of the ends of the multi-filamentary NbTi wires were immersed in liquid tin at 350 °C for 30 min, then in the $(In_{50}Bi_{15})Sn_{35}$ solder at 300 °C for

30 min. 15 mm of solder was then melted in a 2.13 mm diameter cylindrical brass mould at 100 °C, and the wire ends were added to this to form a termination type joint. The complete cast joint was allowed to cool slowly in air. The soldered joint was mounted on a short-straight geometry sample holder, with the joint aligned perpendicular to the applied field. Current was provided using an Agilent 6680A power supply and voltage detected with a Keithley 2182A nanovoltmeter. Critical current values were extracted from I—V plots using a 1 microvolt criterion.

3. Results and discussion

The mono- and multi-filamentary NbTi wires were put in contact with liquid tin to etch away the outer Cu coating and expose the filaments. This interaction was conducted at 350 °C for various times up to a maximum of 1 h to examine the solid–liquid interface at different stages of etching since this process defines the surface of the NbTi filaments that will subsequently be in contact with the liquid solders. Fig. 1a shows the cross-section of the mono-filamentary NbTi wire before and after the tinning process, and Fig. 1b and c shows the state of the NbTi–Sn interface after 2 min and 1 h, and so compares the initial and later stages of interaction. The formation of Cu_6Sn_5 at the Cu—Sn interface was noticed after 2 min of interaction, as shown in Fig. 1b. Cu_6Sn_5 is the first phase to form in the Cu—Sn system and details on the initial stages of formation of this phase have been previously studied in [15]. Most of the Cu was etched away after about 5 min. Importantly, no discernible reaction layer was detected at the NbTi–Sn interface even after an interaction time of 1 h, as shown in Fig. 1c. This is crucial for an understanding of the interaction behaviour between solid NbTi and liquid lead-free solders. We will first discuss results on the development of reaction zones with binary InSn solder after the tinning process for both mono- and multi-filamentary NbTi, followed by similar experiments with ternary (In,Bi)Sn.

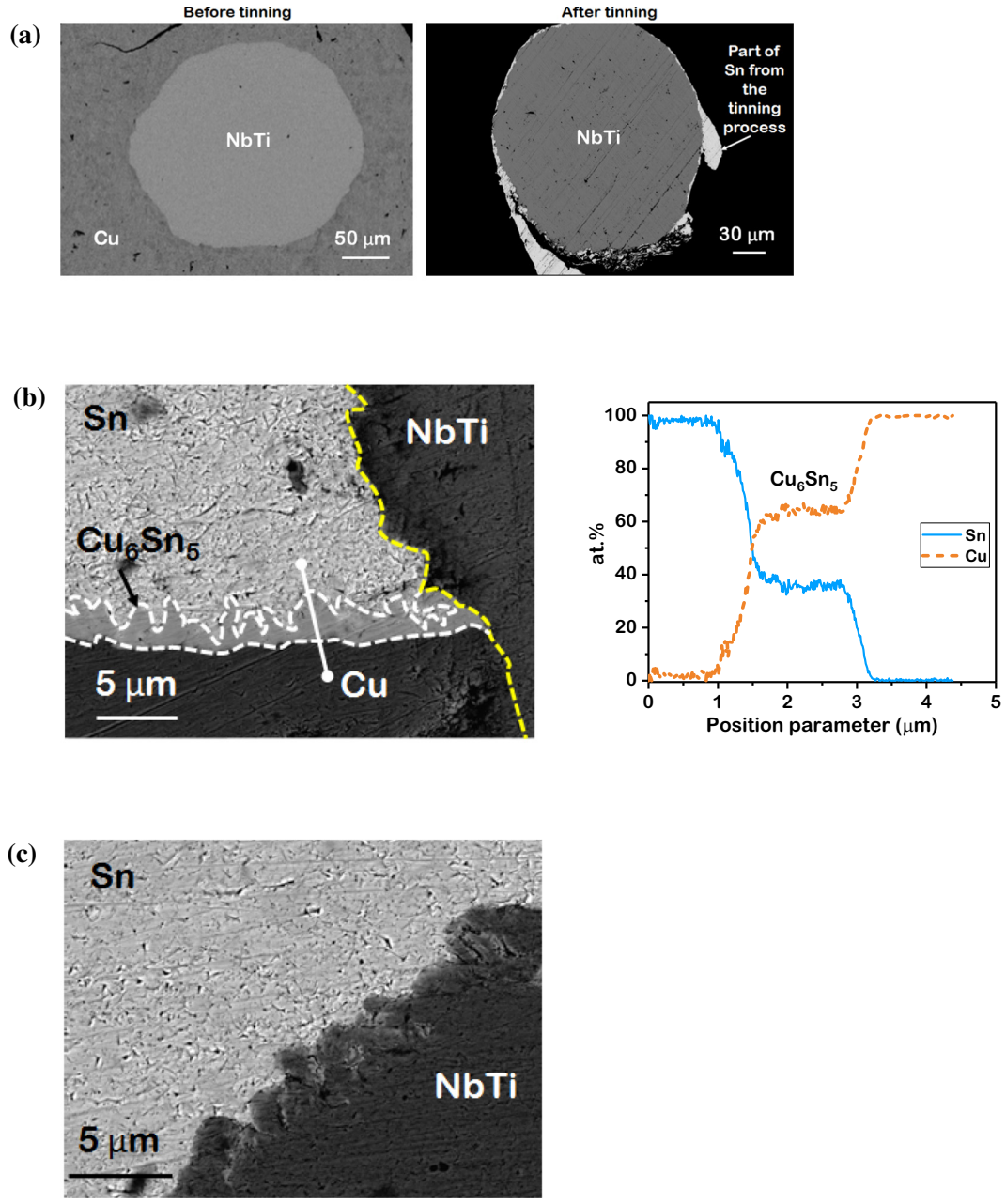

Fig. 1. Back-scattered electron (BSE) micrographs showing (a) the cross-section of the mono-filamentary NbTi wire before and after the tinning process, (b) the formation of Cu_6Sn_5 at the Cu—Sn interface after reaction of Cu-clad mono-filamentary NbTi with liquid Sn at 350 °C for 2 min (along with a composition profile across the Cu—Sn interface as shown by a white straight line on the micrograph), and (c) the lack of a similar interaction zone at the NbTi–Sn interface after 60 min of reaction.

3.1. Solid NbTi–liquid InSn interactions

3.1.1. Phase evolution for different NbTi filaments

The variation in the thickness of the reaction layers developed at the mono-filamentary NbTi-liquid InSn interface at 350 °C after different times is shown in Fig. 2a, and Fig. 2c shows for different temperatures after 268 h. A $NbSn_2$ layer containing Nb: 32 ± 0.3 at.%, Sn: 63 ± 0.5 at.% (2–5 at.% Ti and 4 ± 0.2 at.% In) develops at 350 °C and above, but was not observed at lower temperatures. Noting the solubility of In in the product phase layer, $NbSn_2$ is the lowest-melting Sn-rich phase in the binary Nb—Sn [16] and Ti—Sn [17] systems, and it is not unusual to find the phase rich in the lowest-melting point element forming first in similar solid-liquid interactions [18–20]. The $NbSn_2$ phase grows to a thickness of about 0.5 μm and 4 μm after longer

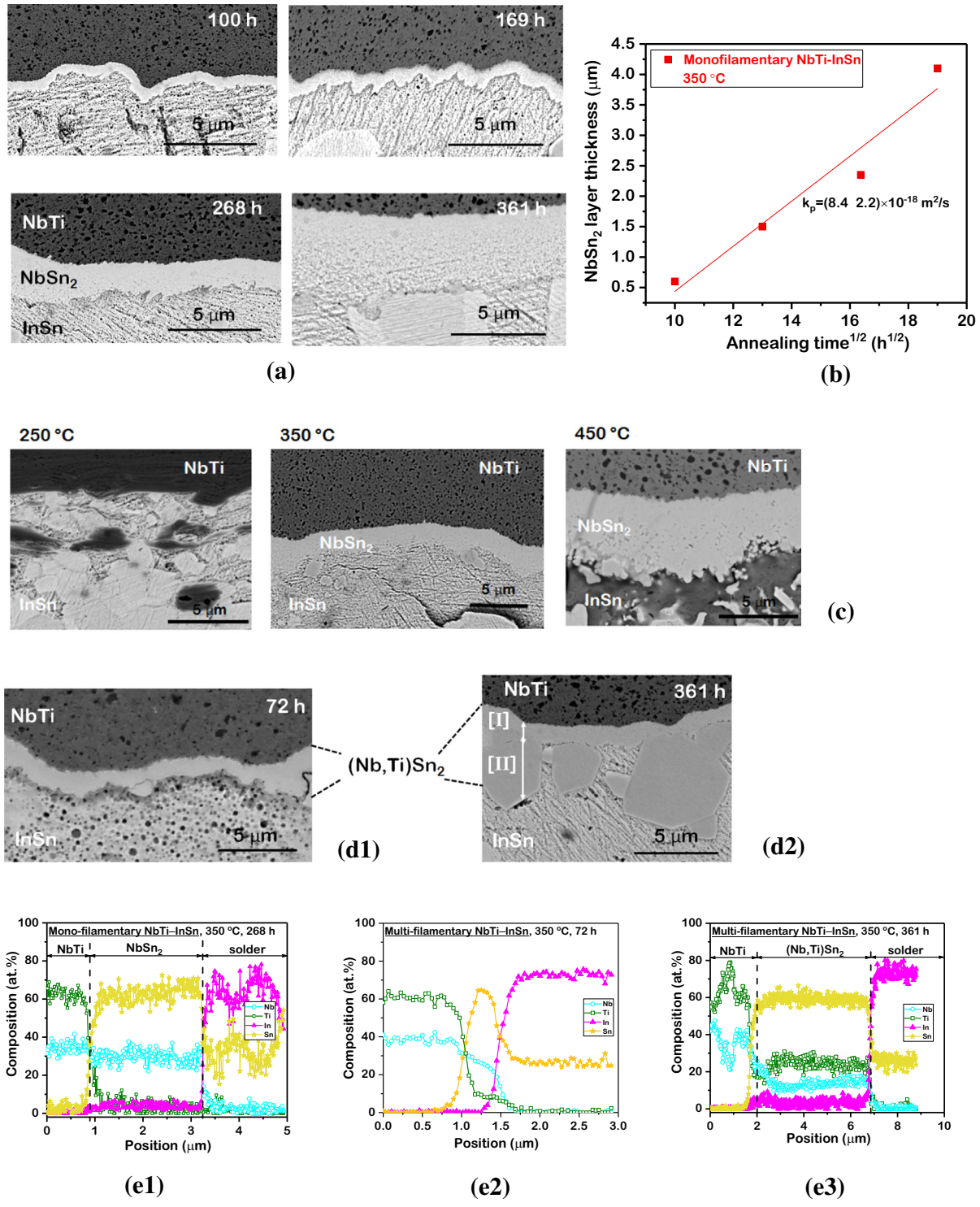

Fig. 2. Back-scattered electron (BSE) micrographs illustrating the interaction zones developed in (a-c) mono-filamentary NbTi–liquid InSn solder interfaces along with the growth plot, (d1,d2) multi-filamentary NbTi–liquid InSn solder interfaces after reaction at 350 °C for different times and (e1–e3) Energy dispersive X-ray (EDX) composition profiles across the interaction zones developed in mono-filamentary NbTi–InSn solder interfaces reacted at 350 °C for 268 h, and multi-filamentary NbTi–InSn solder interfaces reacted at 350 °C for 72 h and 361 h.

reaction times of 100 h and 361 h respectively, and the growth kinetics at 350 °C is plotted in Fig. 2b. Sluggish growth of the $NbSn_2$ phase at the interface between solid Nb and liquid $In_{52}Sn_{48}$ eutectic solder was also reported in two previous studies over the lower temperature range 130–260 °C for prolonged interaction times up to a year [21,22].

Interaction of multi-filamentary NbTi with liquid InSn solder produces the same product phase $NbSn_2$, but with differences in both morphology and composition. Fig. 2d1–d2 presents the evolution of the product phase as a function of annealing time, and at longer times shows a morphology quite different to that developed on mono-filamentary NbTi. A shorter interaction time of 72 h produces only a thin uniform $(Nb,Ti)Sn_2$ phase layer, similar to that of the mono-filament, although this product phase shows a much higher solubility of ~10 at.% Ti. This can be seen by comparing the composition profiles across the interaction zones presented in Fig. 2e1–e3 for mono- and multi-filamentary samples. After 361 h at 350 °C, large scallop-like grains of $(Nb,Ti)Sn_2$ grew on top of the thin continuous layer, again with significantly higher solubility of Ti. A Nb:Ti ratio of 6:1 in the new phase on the mono-filament and 0.4:1 on the multi-filamentary sample can be estimated from the composition profiles in Fig. 2e1 and e3. The Sn content is more or less the same on both mono- and multi-filamentary samples. To the authors' knowledge, no Nb-Ti-Sn isotherm has been established at low temperatures where $NbSn_2$ is a stable phase. From our experimental results, we conclude that the $NbSn_2$ phase with a maximum solubility of ~25 at.% Ti is stable at 350 °C, and that Ti substitutes for Nb on the Nb-sublattice of the $NbSn_2$ because no binary Ti—Sn compound is stable at a composition corresponding to ~66 at.% Sn [17].

The elemental distribution maps (see graphical abstract) also show that significantly more Ti is dissolved in $(Nb,Ti)Sn_2$ at the expense of Nb during the interaction of InSn solder with the multi-filamentary NbTi than in the mono-filamentary sample. Moreover, an increase in the Ti content in the $NbSn_2$ from 10 at.% after 72 h to 20 at.% after 361 h suggests that the multi-filamentary NbTi–$(Nb,Ti)Sn_2$ interface remains in metastable equilibrium at least at shorter times (compare Fig. 2e2 and e3). It is possible that the mono-filamentary sample which shows a solubility of only ~5 at.% Ti in the $(Nb,Ti)Sn_2$ would reach an equilibrium state along the NbTi–$(Nb,Ti)Sn_2$ tieline at much longer interaction times than we explored in this work. Therefore, we attribute the compositional differences in $NbSn_2$ formed on mono- and multi-filamentary NbTi to the time required for the NbTi–$(Nb,Ti)Sn_2$ interface to equilibrate in the two cases, and this may be influenced

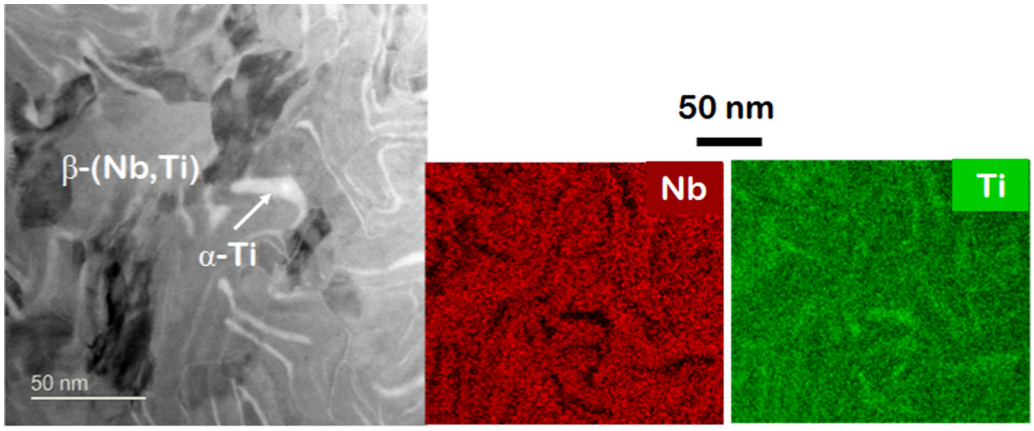

(a)

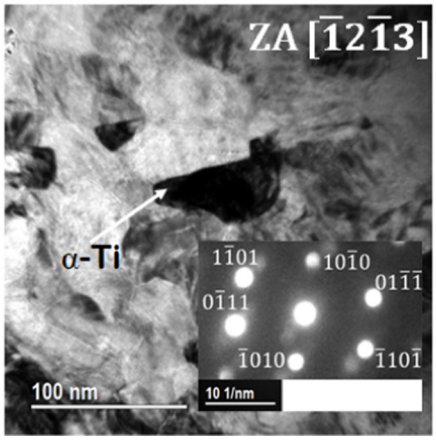

(b)

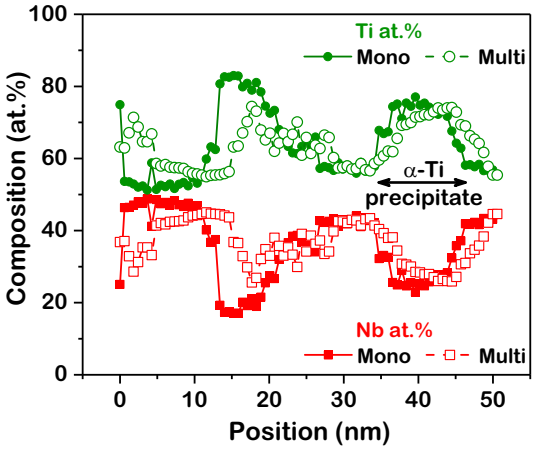

(c)

Fig. 3. (a) Dark-field scanning transmission electron microscopy (STEM) image from the as-received mono-filamentary NbTi with typical EDX maps for Nb and Ti, and (b) bright-field image from the as-received multi-filamentary sample with an inset diffraction pattern acquired from a strongly diffracting α-Ti grain (arrowed). (c) EDX maps and composition gradients measured across the precipitates in mono- and multi-filamentary NbTi samples.

by differences in the metallurgical state of the two filament types investigated. Qualitatively, we expect the free energy of the multi-filamentary NbTi material to be increased by the increased cold work (greater drawing strain) and surface energy (smaller radius of curvature than the mono-filament by a factor of five) both of which will encourage nucleation of $NbSn_2$ grains. The experimental results show a distinct $NbSn_2$ interfacial phase layer after only 72 h of interaction with the InSn liquid for the multi-filamentary NbTi but no discernible $NbSn_2$ layer on the mono-filamentary material (figure is not shown).

Since these interactions have been conducted with solder in the liquid state, it is possible that some of the product phase may detach and be dispersed in the solder, making it difficult to estimate the exact thickness of the product phase. Even so, measuring the thickness of the (Nb,Ti)Sn_2 layer which remains intact on the NbTi filaments, we can state that as well as the observed difference in composition, the growth kinetics of (Nb,Ti)Sn_2 is faster on the finer NbTi filaments than on the large mono-filaments. This encourages us to explore the effect of the different metallurgical states of NbTi on growth in the interaction zone, which in turn may affect the superconducting properties across the interface.

3.1.2. Growth mechanism of (Nb,Ti)Sn_2 in the NbTi–InSn system

Fig. 3a shows annular dark field scanning transmission electron microscopy (STEM) image from the as-received mono-filamentary NbTi sample and the corresponding quantitative EDX mapping. The white ribbon-like features running throughout the sample are the well-known α-Ti precipitates. Fig. 3b shows a bright field image from a typical region of the as-received multi-filamentary sample, and the inset diffraction pattern acquired from one α-Ti precipitate which can be indexed with zone axis $[\bar{1}2\bar{1}3]$ consistent with the hexagonal close-packed (HCP) structure of α-Ti. Fig. 3c compares the composition profiles determined using scanning transmission electron microscopy (STEM) analysis across Ti precipitates from the samples with two different NbTi filaments sizes, and demonstrates that in both the mono- and multi-filamentary samples the β-NbTi matrix has a very similar composition, approximately Nb(60 ± 0.6 at.% Ti).

We also examined the grain size in the β-(Nb,Ti) phase which may strongly influence the diffusion flux of Ti through grain boundaries, and as a consequence through the (Nb,Ti)Sn_2 layer. Fig. 4a presents the EBSD phase map of a region from the as-received mono-filamentary NbTi that exhibits a fine substructure of α-Ti and numerous equiaxed grains of β-(Nb,Ti) forming the continuous superconducting matrix. The normal orientation maps presented in Fig. 4b show a strong crystallographic texture in the β-(Nb,Ti), and exhibits the characteristic ⟨110⟩ deformation fibre texture in a drawn BCC material [23,24]. The (110) pole figure of β-(Nb,Ti) and the $(01\bar{1}1)$ pole figure of HCP α-Ti (Fig. 4c) indicate that one of the preferred orientation relationships between these two phases is $(011)_{BCC}||(01\bar{1}1)_{HCP}$, a Potter orientation relationship in the BCC-HCP system [25]. The grain sizes were estimated using the equivalent circle diameter (ECD) method [26] in the β-(Nb,Ti). The grain size distribution plot in Fig. 4d shows that a significantly higher fraction of the β grains in the as-received multi-filament lie in the range from 5 to 25 nm than in the mono-filament. The average grain size was determined to be 40 ± 0.8 nm in the case of the mono-filamentary sample and 22 ± 0.3 nm for the multi-filamentary sample that has experienced almost 95% higher deformation strain. These much finer β-(Nb,Ti) grains in the multi-filamentary NbTi sample

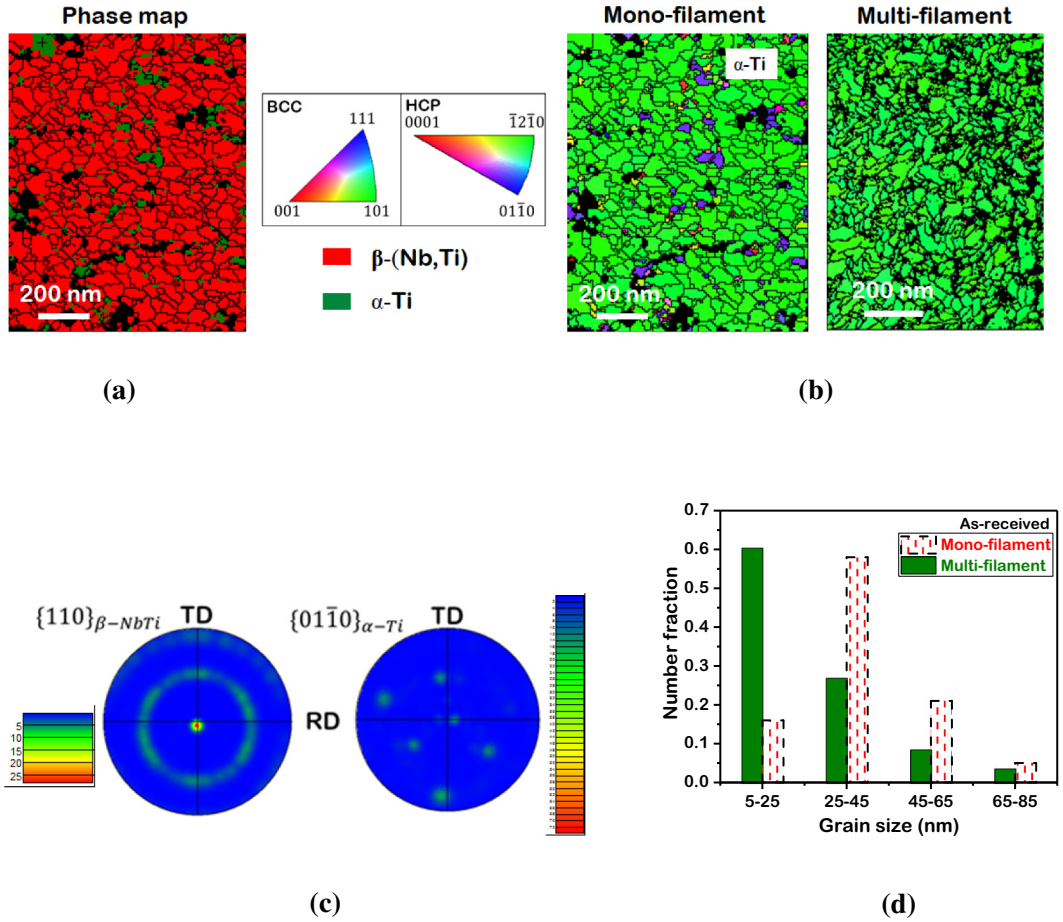

Fig. 4. (a) Transmission Kikuchi diffraction (TKD) phase map of the as-received mono-filamentary NbTi, (b) orientation maps (|| ND) of the as-received mono- and multi-filamentary NbTi samples. (c) (110) pole figure of β-(Nb,Ti) and $(01\bar{1}1)$ pole figure of α-Ti and (d) β-(Nb,Ti) grain size distribution in the NbTi materials.

could encourage the formation of (Nb,Ti)Sn_2 when interacting with the liquid InSn solder by offering a kinetic advantage from the high density of fast reaction paths and also a large number of high energy sites for the nucleation of intermetallic grains. To have a better understanding of the growth behaviour in these two cases, the microstructural evolution of the product phases was compared and the growth mechanism analysed.

A close inspection of the interaction zone developed at 450 °C for 268 h on the mono-filamentary NbTi has revealed the presence of a line of pores inside the product phase, demarcated by white arrows in Fig. 5a. These voids indicate the location of the Kirkendall plane (K-plane) that gives an indication of the relative mobility of the elemental species. From the composition profiles in Fig. 2e1 In has almost negligible solubility in the $NbSn_2$, and there is also no detectible Ti diffusion through the growing intermetallic phase towards the $NbSn_2$–InSn interface (Fig. 2e1) so that we can infer that the growth of $NbSn_2$ occurs primarily by the diffusion of Nb and Sn. The diffusion-controlled nature of planar growth of any reaction phase layer can be demonstrated by plotting the parabolic growth curve [27]. The $NbSn_2$ layer thickness as a function of (annealing time)$^{1/2}$ plot for the mono-filamentary NbTi–InSn interaction is shown in Fig. 2b, and it closely follows parabolic growth behaviour. For short annealing times or slow growth rate of the reaction zone, the growth constant does not deviate much from 0.5 for axial geometry wires [27]. Diffusion-controlled growth of $NbSn_2$ has also been reported in previous work on Nb–$In_{52}Sn_{48}$ interactions [21,22]. Often the microstructural evolution of the product phase can help elucidate its growth mechanism in systems governed by solid-state diffusion-controlled growth [28]. An EBSD scan across the interaction zone on the mono-filamentary NbTi, Fig. 5b, shows a duplex morphology in the $NbSn_2$ phase. Smaller $NbSn_2$ grains are present closer to $NbSn_2$–NbTi interface (interface [i]), while towards the InSn–$NbSn_2$ interface (interface [ii]) coarser grains have grown. Fig. 5c shows that region [I] contains a higher fraction of finer grains (50–250 nm), and most of the grains ranging from 250 nm to 850 nm are present in region [II]. The Kirkendall plane demarcates the interface between the two sublayers comprising finer and coarser grains. Following the approach that relates the diffusion rate of different components with the microstructural characteristics of the interaction zone [29], we can suggest

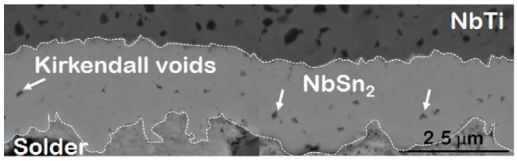

(a)

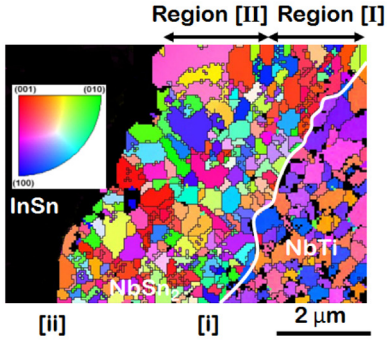

(b)

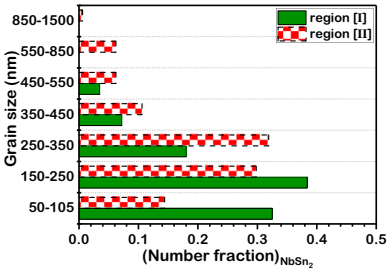

(c)

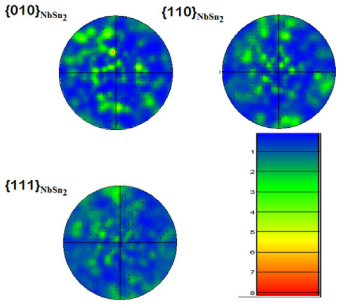

(d)

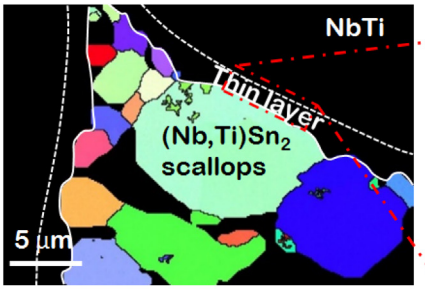

(e1)

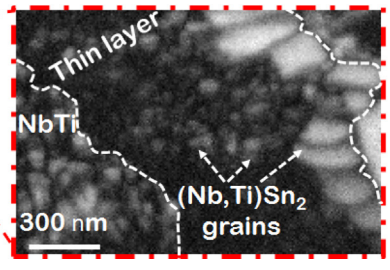

(e2)

Fig. 5. (a) BSE micrograph illustrating the Kirkendall voids inside the $NbSn_2$ phase layer formed by reaction of mono-filamentary NbTi with liquid InSn, (b) orientation map of a similar region, (c) grain size distribution histogram of two different regions in the $NbSn_2$ phase layer, and (d) pole figures of $NbSn_2$. (e1, e2) EBSD map of a scalloped region formed by reaction of multi-filamentary NbTi with liquid InSn along with a band contrast map illustrating the smaller grains in the thin (Nb,Ti)Sn_2 layer (highlighted by white dashed arrows).

that the sublayer between interface [i] and the K-plane grows by diffusion of Sn through $NbSn_2$ to react with Nb, while the other sublayer between the K-plane and interface [ii] grows by diffusion of Nb towards the solder. The position of the K-plane more or less at the middle of the product phase suggests comparable diffusion rates for Nb and Sn. It is interesting to compare these observations with the growth of the A15 superconducting intermetallic Nb_3Sn by the reaction of tin with Nb at higher temperatures, which has been described by a similar scenario [30]. Nb has a higher diffusion rate through Nb_3Sn because of greater number of Nb—Nb bonds, while the transport of Sn was attributed primarily to grain boundary diffusion. In a similar way, crystallographic analysis of $NbSn_2$ can help to understand the atomic mechanisms of diffusion in our samples.

$NbSn_2$ crystallizes in a complex face-centred orthorhombic structure with 48 atoms in a unit cell (Pearson symbol: oF48, space group: Fddd) [22], as displayed in Fig. 6 where the unit cell showing the nearest neighbours of Nb and Sn atoms has been constructed using the CrystalMaker software [31]. The unit cell consists of one Nb and two Sn sublattices (designated as Sn_I and Sn_{II}) with similar atomic occupancies. Each Nb atom has 2 Nb and 8 Sn atoms (4 Sn_I and 4 Sn_{II}) as nearest neighbours, while Sn_I is surrounded by 11 Sn (3 Sn_I and 8 Sn_{II}) and 4 Nb atoms, and Sn_{II} is a neighbour to 11 Sn (8 Sn_I and 3 Sn_{II}) and 4 Nb atoms. This means that if vacancies are present on both sub-lattices, both Nb and Sn atoms can diffuse by making jumps via their own sub-lattices since each species has like atoms as nearest neighbours. At first glance, Sn appears likely to show a higher diffusion rate because it has a significantly larger number of Sn—Sn bonds, compared to just two Nb—Nb bonds. The dominant diffusing species is the majority one in metal-disilicides such as VSi_2, $HfSi_2$ and $MoSi_2$ [32] and other AB_2-type compounds, for example $CuAl_2$ [33] and WPt_2 [34]. For the formation of Nb_3Sn, the faster diffusing component is also the majority species, Nb [30,35]. On the contrary, Hong and d'Heurle [36] demonstrated the minority atom (Cu) to diffuse faster than Mg in $CuMg_2$, a structural prototype of $NbSn_2$, and attributed the higher diffusion rate of the minority atom to the two continuous chains of Cu atoms oriented at an angle of 60° in the unit cell of the $CuMg_2$-type structure. The similar long chains of the minority Nb atoms in the unit cell of $NbSn_2$ are identified in Fig. 6. However, this kind of argument based on the likelihood of atomic site jumps is only relevant if lattice diffusion is the dominant mechanism during the growth of $NbSn_2$. Given the melting point of $NbSn_2$ is 850 °C [16], the homologous temperature of the solder interactions studied here lies in the range 0.5–0.6 and we would expect both lattice and grain boundary diffusion to contribute to an overall growth process, especially given the fine grain size of 250 ± 10 nm. These $NbSn_2$ grains do not exhibit any preferred crystallographic growth direction as shown by the (001), (101) and (111) pole figures in Fig. 5d. Hence, many $NbSn_2$ grains nucleate with random orientation on the $NbSn_2$–NbTi interface, thereby weakening the inheritance of any strong crystallographic texture from the NbTi, and resulting in a high concentration of high angle grain boundaries which should be efficient diffusion paths.

In the case of solder reaction with the multi-filamentary NbTi, two distinct sublayers were noticed, as shown in Fig. 2d2, with a thinner sublayer [I] towards the NbTi and a thicker one [II] towards the InSn. Fig. 5e1 shows only the microstructural features of sublayer [II] since the grains in sublayer [I] were too fine for bulk EBSD analysis. However, the band contrast map shows details of this very fine grain structure in sublayer [I] in the area enclosed by white dashed lines in Fig. 5e2. There are very small equiaxed $(Nb,Ti)Sn_2$ grains close to the NbTi filament which transform to larger columnar grains as they grow towards the solder, both indicated by white dashed arrows. It is apparent from the composition profile (Fig. 2e3) that a significant amount of Ti is present in sublayer [II], suggesting Ti participates along with Nb and Sn in the growth of $(Nb,Ti)Sn_2$, in contrast to the low Ti concentration in the product phase on the mono-filamentary sample (Fig. 2e1). As mentioned above, the number of potential nucleation sites for $(Nb,Ti)Sn_2$ is expected to be higher on the surface of the multi-filamentary NbTi with a finer microstructure, resulting in the much smaller average grain size (approximately 30 nm) in sublayer [I] adjacent to the NbTi, Fig. 5e2. These finer grains would then provide a large grain boundary area to facilitate a greater diffusion flux of Ti. As a result of the higher activity of Ti in the multi-filamentary NbTi, we also find a higher concentration of Ti in the interfacial product layer, $(Nb,Ti)Sn_2$. Although the observation of very small $(Nb,Ti)Sn_2$ grains in sublayer [I] suggests a low barrier for grain nucleation immediately at the $(Nb,Ti)Sn_2$–NbTi interface, the more columnar microstructure that develops subsequently suggests that nucleation is suppressed further from the NbTi surface and growth of the $(Nb,Ti)Sn_2$ is by diffusing metal atoms joining preferentially to the surface of existing grains, and that it is the combined flux of Nb and Ti that controls the rate of growth of sublayer [II].

The interfacial layers formed by reaction with the InSn solder have two different morphologies on the mono- and multi-filamentary samples (Fig. 5), and growth mechanisms for the growth of these layers

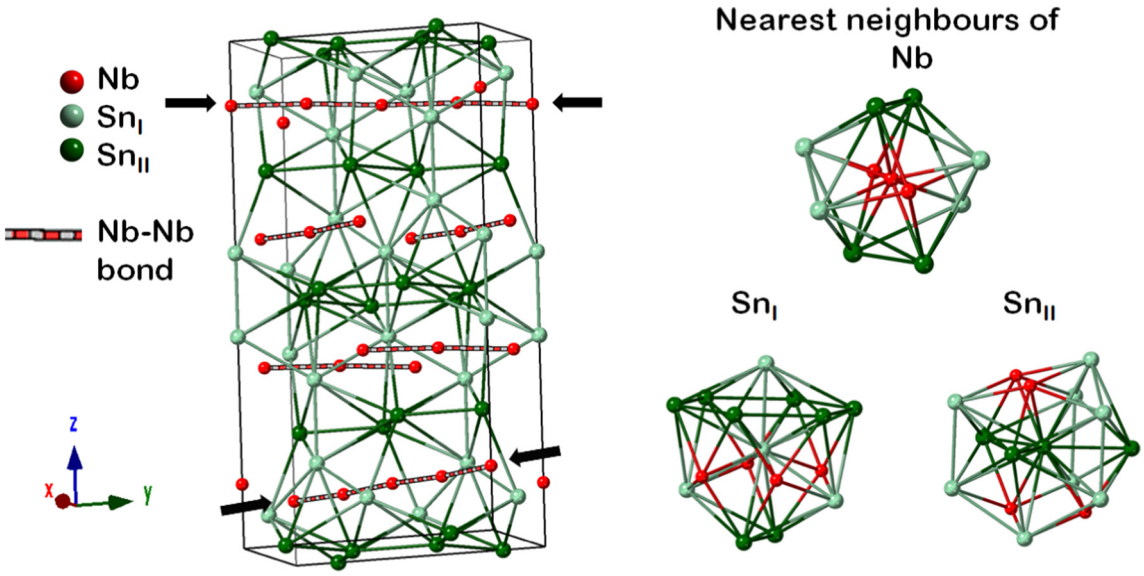

Fig. 6. Crystal structure of $NbSn_2$ and nearest neighbours of Nb and Sn atoms.

can be proposed with the help of the schematic diagram shown in Fig. 7. Fig. 7a illustrates the growth of $NbSn_2$ on the mono-filamentary NbTi. The lack of either In or Ti (Fig. 2e1) combined with the presence of a clear Kirkendall plane in the $NbSn_2$ layer (Fig. 5a) suggest that diffusion of both Nb and Sn contribute to the growth of a polycrystalline $NbSn_2$ layer on the mono-filamentary NbTi by repeated nucleation of new, randomly oriented grains on both sides of the intermetallic layer. The morphological evolution of the interfacial $(Nb,Ti)Sn_2$ phase layer on the multi-filamentary sample is sketched in Fig. 7b to take place in three steps. Step 1 ($t = t_1$) in Fig. 7b shows the nucleation of a thin continuous layer of small, randomly oriented $(Nb,Ti)Sn_2$ grains on the NbTi surface (Fig. 2d1) – a similar microstructure to that developed in the early stages on the mono-filamentary NbTi. However in step 2 ($t = t_2$), the growth of this $(Nb,Ti)Sn_2$ layer is now into the smaller pockets of InSn solder trapped between the individual filaments, and this solder is rapidly depleted in Sn. The resulting reduced Sn concentration gradient near the $(Nb,Ti)Sn_2$–InSn interface will limit the supply of Sn atoms to diffuse through the growing intermetallic layer, $(Nb,Ti)Sn_2$, and suppress further nucleation of new $(Nb,Ti)Sn_2$ grains at the $(Nb,Ti)Sn_2$–NbTi interface. The primary growth mechanism will then be at the $(Nb,Ti)Sn_2$–InSn interface, where diffusing Nb and Ti atoms react with what Sn is available at the surface of existing $(Nb,Ti)Sn_2$ grains. The local supersaturation is not high enough to overcome the activation barrier to form new grains, leading to the formation of a columnar grain structure. Duplex morphology comprising of columnar and equiaxed grains was also observed for the Nb_3Sn phase in the Nb–Cu(Sn) system with the columnar grains at the Nb–Nb_3Sn interface and equiaxed grains at the interface, Nb_3Sn–Cu(Sn) [37]. In the Nb–Cu(Sn) system, the Nb_3Sn grains nucleate only at the Nb surface when Sn from Cu(Sn) dissociates and reacts with Nb, and further, growth of the Nb_3Sn phase layer continues by the diffusion of Sn along the grain boundaries of Nb_3Sn [38]. Okuda et al. [37] attributed the presence of equiaxed Nb_3Sn grains for smaller annealing time to a high Sn concentration in Cu(Sn), which would encourage the nucleation of Nb_3Sn grains at the Nb–Nb_3Sn interface. At the later stage of annealing, low tin concentration in Cu(Sn) would favour the growth of the existing grains with lower nucleation rate, and result in the formation of the columnar grains [37]. At later stages, step 3 ($t = t_3$), diffusion-limited growth of Nb and Ti through the thicker $(Nb,Ti)Sn_2$ layer reduces the driving force further, re-nucleation will be very unlikely and only a few of the $(Nb,Ti)Sn_2$ grains will have surfaces sufficiently mobile to continue to grow, leading to coarsening of the intermetallic grain structure and formation of the scalloped structures.

3.1.3. Effect of soldering with InSn on the superconducting properties of NbTi

The elevated temperature during the joining of two NbTi superconducting wires by soldering may influence the microstructure of the NbTi matrix and in turn the superconducting properties [39]. In our experiments, the measured higher concentrations of Ti in the $(Nb,Ti)Sn_2$ formed on the multi-filamentary sample suggests that the rate of loss of Nb and Ti from the mono-filamentary and multi-filamentary NbTi is different, and the different ratios of Nb:Ti in the product phases on the two NbTi conductors sizes is an additional factor we can study.

The superconducting properties of NbTi filaments in as-received (AR), heat treated (HT) and soldered (S) conditions have been compared for both mono- and multi-filamentary samples after an annealing treatment at 350 °C for 169 h. The AR sample refers to the as-received filaments from which the outer Cu stabilizer coating has been removed by the tinning process as discussed above. As a reference, an unsoldered filament has been heat treated (HT) by removing the Cu coating followed by annealing in vacuum to prevent oxidation. This sample is to allow us to separate (a) changes in the microstructure from long term annealing that may contribute to modification of pinning in the NbTi filaments from (b) the introduction of a new pinning landscape on the surface of the filaments from reactions with the solder. The critical temperatures (T_c) at different magnetic fields ranging from 1 to 100 mT and the critical current densities (J_c) at 4.2 K were estimated from the measured M-T (moment-temperature) plots and M-H (moment-magnetic field) loops, respectively. The M-T plot at 1 mT for the AR, HT and S mono-filamentary samples is shown in Fig. 8a. The T_c values were found to be unchanged at 9.2 K in magnetic fields up to 100 mT for all the AR, HT and S samples.

Fig. 8b and c illustrate the variations in measured critical current density values with applied magnetic field for mono- and multi-filamentary samples respectively. J_c values for all the samples were calculated using the Bean formula (Eqs. (1) and (2)),

$$J_c = \frac{3\Delta M}{2r_f} \tag{1}$$

where r_f is the filament radius and ΔM is the hysteresis loop width in the M-H loops. For multi-filamentary conductors we approximated the signal as the sum of n individual filaments,

$$J_c = \frac{3\Delta M}{2r_f n} \tag{2}$$

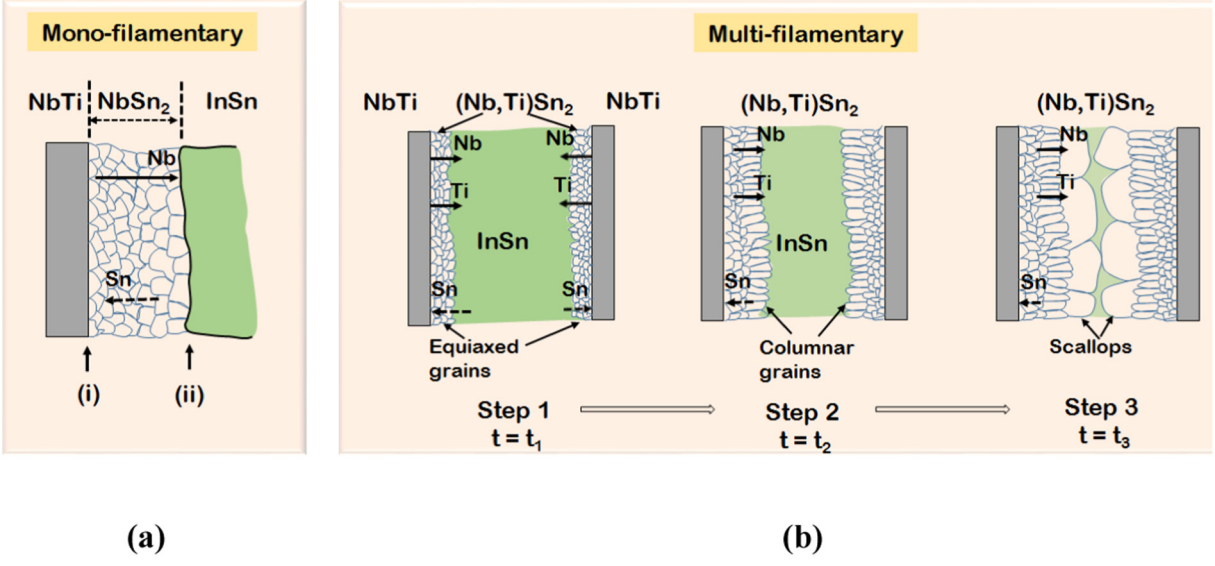

Fig. 7. Schematic illustration of development of the interfacial phase layers in the mono- and multi-filamentary NbTi samples on interaction with the binary InSn solder.

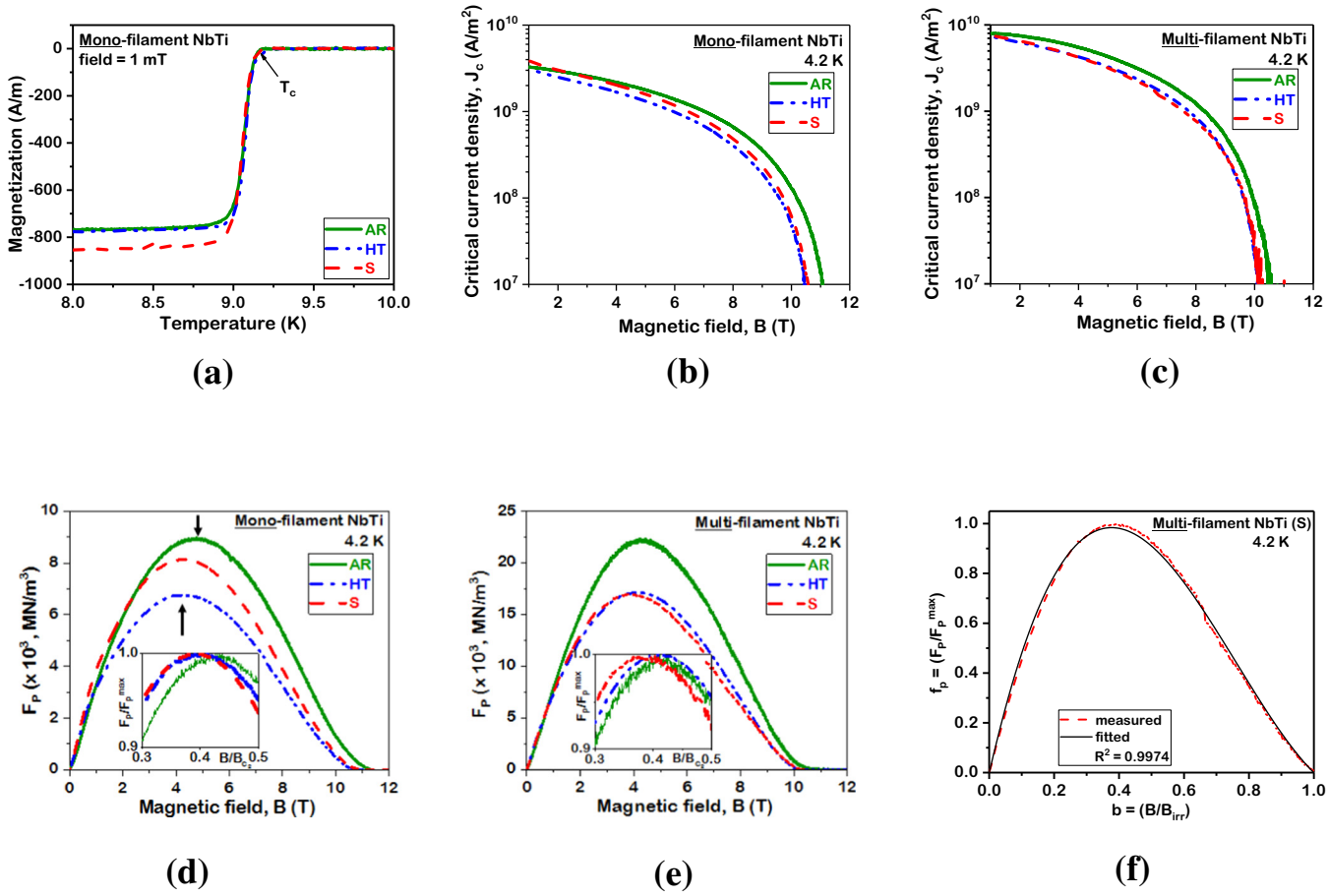

Fig. 8. Superconducting properties of as received (AR), heat treated (HT) and soldered (S) mono- and multi-filamentary samples. (a) M-T plot for the mono-filamentary NbTi samples, (b and c) Variation of J_c and (d and e) F_p with magnetic field in mono- and multi-filamentary NbTi samples respectively. The inserts in (d) and (e) show details of the peak in the pinning curve. (f) Fitting of the normalized pinning force density-reduced field curve for the soldered multi-filamentary NbTi sample using a two-component model.

where n is the number of filaments in the conductor and r_f is the radius of an individual filament. The J_c values for the HT and S samples in both mono- and multi-filamentary materials show a significant decrease, presumably because the prolonged annealing treatment encourages coarsening of the α-Ti precipitates which are believed to be the major flux-pinning sites [39,40]. In addition, the irreversibility fields (B_{irr}) of both HT and S samples have decreased compared to AR for both mono- and multi-filamentary samples. The irreversibility field (B_{irr}) is determined from the $J_c - B$ plots, and the value is chosen at $J_c = 10^7$ A/m^2. This reduction in B_{irr} can be attributed to stress-relief and annihilation of defects such as dislocations introduced during the drawing stage of manufacture of the filamentary wires. Therefore, the simulated long soldering process affects both critical current density as well as the irreversibility field of the NbTi filaments.

The pinning properties of NbTi may also be affected by soldering, and this has been examined by measuring the dependence of the global pinning force density (F_P) on the applied magnetic field, described using Eqs. (3).

$$F_P = B \times J_c \tag{3}$$

This can be quantified experimentally as a function of the applied magnetic field from the $J_c - B$ plots shown in Fig. 8d and e. On comparing the F_P values for the AR, HT and S samples for mono-filamentary NbTi we note that the maximum F_P value has reduced by 10% and 22% for the S and HT samples respectively, and by 24% for the S and HT multi-filamentary samples. Reduction in F_P is again presumably as a result of the annealing out of defects that act as pinning sites. However, the less severe reduction in F_P in the S sample may suggest that diffusional interactions with the InSn solder generate additional pinning centres to offset the annealing effect, but that these new centres are less effective in the multi-filamentary NbTi sample. The effect of annealing temperature on the pinning force density of multi-filamentary NbTi wires was previously studied [41]. The authors found F_P to decrease by ~35% after annealing from 390 °C to 550 °C for 2 h, and a shift in the peak position of F_P towards lower magnetic fields. Although the time for the heat treatment processes in our study is 169 h, the annealing temperature is 350 °C, which is lower than either of the temperatures used in [41]. Since the influence of temperature is expected to be stronger than the heat treatment time, the behaviour of F_P as a function of heat treatment variables obtained in the present study looks in good conformity with the previously reported ones [41]. In our study also, we find a small shift in the position of the peak of the pinning force density to lower fields after the heat treatment processes in the mono-filament and multi-filament samples, as shown by the arrows in Fig. 8d and e. The shift in the position of the maximum for the F_P curves indicates a change in the pinning mechanism. The normalized pinning force density $f_p - b$ curves for the AR, HT and S treatments of mono- and multi-filamentary NbTi samples are presented as insets in Fig. 8d and e to make it easier to see the shift of the f_p curve with respect to the reduced field.

The behaviour of the normalized pinning force density ($f_p = \frac{F_P}{F_P^{max}}$) with reduced field, $b = \frac{B}{B_{irr}}$, provides additional insight into these pinning mechanisms. An understanding of the pinning mechanism in a superconductor helps engineering the microstructure of a superconducting material to increase the critical current density (J_c).

The pinning in a superconductor occurs when the flux-lines interact with the pinning centres, and the efficiency of these pinning centres depends on the strength of the interaction. The strength of the interaction depends on the difference in the characteristics of the matrix superconducting phase and the pinning centre. The two most important factors responsible for the flux-pinning in a superconductor has been identified as: (i) $\Delta\kappa$-*pinning* associated with the change in the Ginzburg-Landau parameter due to composition fluctuations and (ii) *normal pinning* (*N-pinning*) because of the presence of non-superconducting phases [42]. The strength of each individual pinning mechanism depends on the dimensionality of the pinning centre compared to the inter flux-line length, *d*. The pinning centres are further classified as: (i) point-pins (no dimension > *d*), (ii) line-pins (one dimension > *d*), (iii) surface-pins (two dimension > *d*) and (iv) volume-pins (all dimensions > *d*). More than one pinning mechanism can contribute to flux-pinning in a superconducting material, and to quantify the mechanism, Dew-Hughes developed a mathematical model for a type II superconductor [42].

We have used the Dew-Hughes model for flux-pinning mechanisms [42] and followed the mathematical relation (Eq. (4)),

$$f_p = \left[A \cdot b^p \cdot (1-b)^q\right] \tag{4}$$

where p and q are scaling parameters for a particular pinning mechanism and A represents a weighting factor for each mechanism. A two-component model was used for non-linear curve fitting of the measured $f_p - b$ curves, following Eq. (5)

$$f_p = \left[A_1 \cdot b^{p_1} \cdot (1-b)^{q_1}\right] + \left[A_2 \cdot b^{p_2} \cdot (1-b)^{q_2}\right]. \tag{5}$$

Fitting of the normalized $f_p - b$ curve for the soldered multi-filamentary NbTi sample is shown in Fig. 8f. The fitted values of $p_1 = 1.5$ and $q_1 = 1$ represent surface $\Delta\kappa$-pinning while the values of $p_2 = 1$ and $q_2 = 2$ correspond to point *N*-type pinning. The fitted weighting factors A_1 and A_2 for the results on the mono- and multi-filamentary AR, HT and S samples are listed in Table 1, and indicate both surface $\Delta\kappa$ and point *N*-type pinning to be operative in the mono- and multi-filamentary NbTi samples, with a higher weighting factor for the *N*-type pinning coefficient A_2. Commercial NbTi wires are manufactured to contain fine non-superconducting α-Ti precipitates in a fine-grained matrix of superconducting β-(Nb,Ti) (Fig. 4b), and so strong contributions from both normal point pinning sites (precipitates) and $\Delta\kappa$ surface pinning from the grain boundaries is expected [43].

On comparing the $f_p - b$ and $F_P - B$ curves from the HT and S samples for both mono- and multi-filamentary NbTi, it is clear that the introduction of NbTi–$NbSn_2$ interphase boundaries does not compensate for factors reducing the flux-pinning strength in the soldered NbTi filaments, so changes in the metallurgical state of the NbTi filaments dominate the pinning force, F_P. Most of the studies cite α-Ti precipitates as the major flux pinning sites in the un-treated NbTi wires, including composition gradients across these precipitates, and with the peak of the normalized pinning force density $f_p - b$ curve lying between 0.33 and 0.6 [42,44,45]. Reduction in the concentration gradient across the α-Ti pinning centres has been cited as one of the reasons for a decrease in the irreversibility field and a shift in the maximum of the reduced pinning force density curve towards lower magnetic fields with an increase in annealing time [46,47]. Our results show that the total pinning force density decreases on annealing (Fig. 8d and e) with the coefficient A_2 increasing relative to the A_1. This could suggest that the normal pinning remains largely unchanged but the surface pinning stemming from the β-(Nb,Ti) reduces. It is expected since annealing will cause growth of the β-(Nb,Ti) grains which reduces grain boundary area.

Table 1
Weighting factors A_1 and A_2 for as-received (AR), heat-treated (HT) and soldered (S) mono- and multi-filamentary NbTi samples deduced from the Dew-Hughes flux-pinning model.

Samples	Mono-filament NbTi		Multi-filament NbTi	
	A_1	A_2	A_1	A_2
AR	1.9	4.7	1.8	4.7
HT	1.4	5.4	1.7	5.0
S	1.1	5.7	1.2	5.4

3.2. Interaction of solid NbTi filaments with liquid ternary (In,Bi)Sn

In contrast to the NbTi–InSn interaction where the (Nb,Ti)Sn_2 phase grows at the interface, the interactions of solid NbTi and liquid ternary (In,Bi)Sn solder result in no detectable interaction zone at the solid–liquid interface, as illustrated in Fig. 9a. There could be several reasons for not finding any reaction layer in the case of the ternary solder: (i) the change in the solder chemistry may decrease the nucleation rate of any intermetallic phase, (ii) there may not be any stable reaction product in this range of Bi content in the temperature range 250–450 °C, (iii) the thermodynamic driving force for diffusion (i.e. the thermodynamic factor) of key elements forming the product phase may be severely reduced, or (iv) a decrease in the thermodynamic activity of the reacting elements in the bulk solder. To decide between these possibilities would require detailed thermodynamic data on the quinary In-Sn-Bi-Nb-Ti system, but to the authors' knowledge this is not available in the literature. However, the thermodynamic activities of various elements in (In,Bi)Sn can be estimated from the ternary In-Bi-Sn system.

Using ThermoCalc [48] software, and the Gibbs free energy parameters of the relevant phases based on the work of Witusiewicz et al. [49], and assuming that $NbSn_2$ is the preferred phase at this interface, we concentrate on the thermodynamic parameters of Sn in liquid (In,Bi)Sn solder. The effect of Bi concentration on the thermodynamic activity of Sn in the solder was estimated, as plotted in Fig. 9b, showing a significant decrease over the relevant range of Bi contents. This may have a considerable effect on the driving force for the formation of the $NbSn_2$ product phase at the solid–liquid interface. A similar addition of Bi to lower the activity of Sn in BiSn solder was cited as one of the reasons contributing to a small decrease in the growth rate of Cu—Sn product phases in the Cu–BiSn system [50]. Hence, interfacial reactions in the solid NbTi–liquid (In,Bi)Sn system to form (Nb,Ti)Sn_2 may be suppressed by a reduction in the overall driving force. The NbTi–InSn solder system is very unusual in the sense that most reported metallic substrate–liquid solder systems exhibit interfacial reactions several orders of magnitude faster than we report here [51]. This extremely sluggish reaction behaviour with the addition of Bi to the solder may have important consequences for the superconducting properties of these interfaces.

The lack of any discernible interaction zone in the case of the Bi-containing ternary solder has an added advantage in comparison to binary InSn. The Kirkendall plane observed inside the (Nb,Ti)Sn_2 product phase layer in Fig. 5a would be a preferential failure site under mechanical load, and we have observed that the (Nb,Ti)Sn_2 phase layer remains intact on the NbTi filaments up to a critical thickness of approximately 2 μm, and above this thickness the reaction layer starts detaching from the NbTi filaments and the crystal fragments disperse in the liquid solder (Fig. 2a). This brittle failure may have a serious impact on the long-term reliability of the solder joint. It is interesting that the lead-based $Pb_{60}Bi_{40}$ solder commonly used to create persistent mode joints in the manufacturing of MRI magnets also produces no detectable interaction zone after reaction with NbTi at 350 °C for 100 h, Fig. 9c. These observations on the effect of Bi on solder reactions with NbTi filaments reinforces the idea that the ternary (In,Bi)Sn system may be an attractive choice for lead-free superconducting solder joint materials for LTS materials such as NbTi [9].

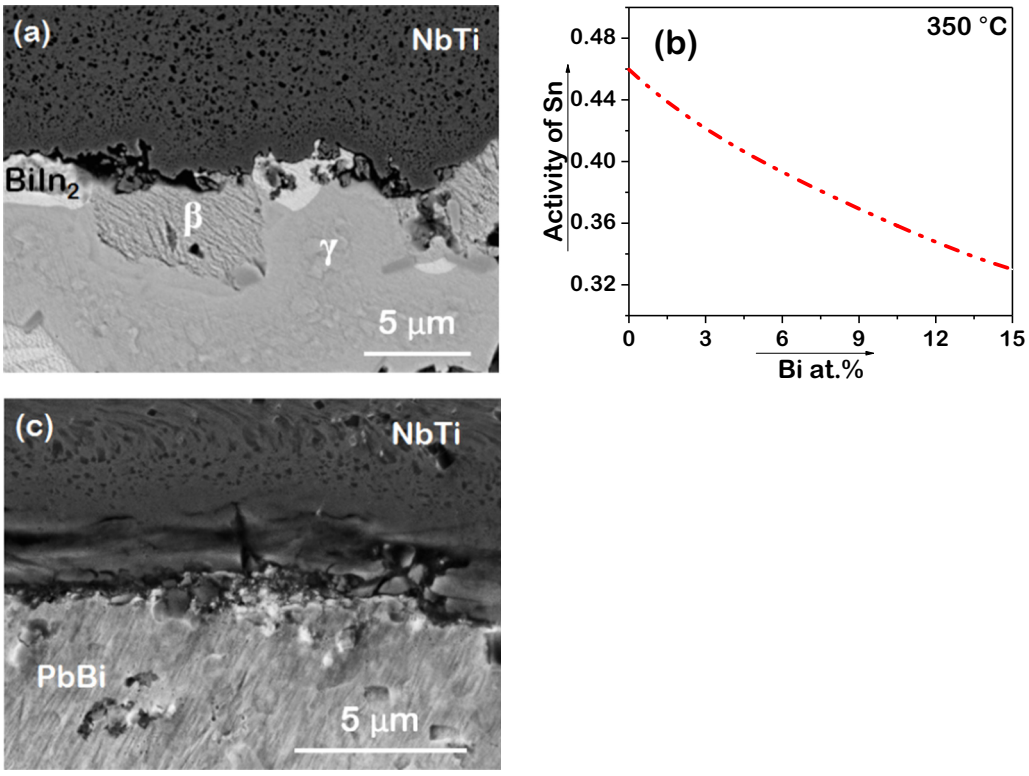

Fig. 9. (a) BSE micrograph showing the NbTi–liquid (In,Bi)Sn solder interface where only the three equilibrium phases present in the ternary solder (β, γ and $BiIn_2$) are detected, and no reaction layer. (b) Estimated variation of the thermodynamic activity of Sn in (In,Bi)Sn as a function of Bi content. (c) BSE micrograph showing the NbTi–liquid PbBi solder interface with no detectable reaction layer.

3.3. Nucleation of the bulk solder phases on NbTi

One of the key requirements of the NbTi–solder joint is that sufficient supercurrent can flow across the joint under typical operating conditions (4.2 K in a field of 1 T for a typical MRI magnet) [1]. The supercurrent that can flow from one NbTi wire to another depends not only on any interfacial reaction layer but also on the specific phases in the bulk solder in contact with the NbTi filaments. The nucleation behaviour of the equilibrium phases in bulk binary and ternary solders at the S–L interface can be explained by correlating the experimental observations with the solidification path predicted by the liquidus line in the appropriate phase diagram.

In Fig. 10a the initial composition of the binary solder is marked as a red dashed arrow on an enlarged section of the In—Sn phase diagram. At the onset of solidification, the In-rich β-In_3Sn phase nucleates first at the S–L interface when the temperature reaches the liquidus line at '*A*'. As a result, the remaining liquid becomes supersaturated with Sn until the eutectic reaction to form β and the Sn-rich γ phase occurs. Thus we would expect immediately around the $NbSn_2$ layer formed at this interface as described above, that most of the interfacial region is

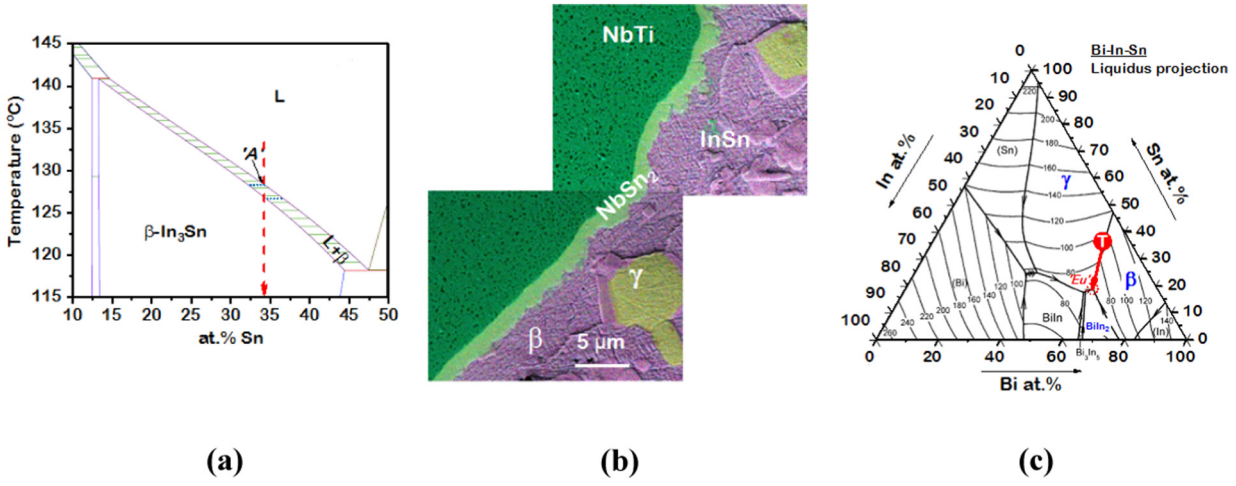

Fig. 10. (a) A detail of In—Sn phase diagram (calculated using ThermoCalc software) showing the starting composition of the binary solder, (b) EDX phase map showing the presence of the β phase in contact with the $NbSn_2$ formed at the NbTi–InSn solder interface in the mono-filamentary sample at 350 °C for 268 h. (c) Liquidus projection of the In-Bi-Sn system [49] depicting the solidification path for the ternary solder.

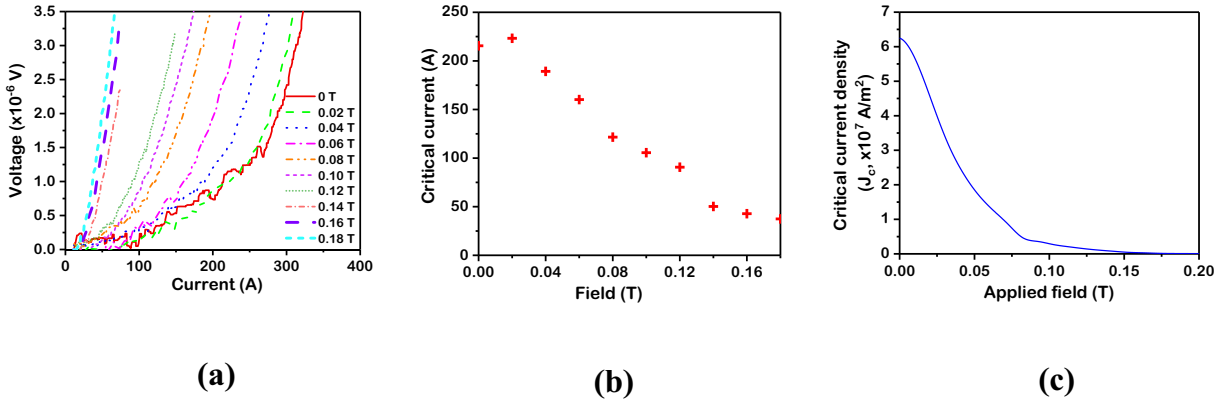

Fig. 11. (a) I—V characteristics of (In,Bi)Sn solder joint, from which (b) the $I_c(B)$ performance was extracted via a 1 microvolt criteria and (c) critical current from magnetisation of slow-cooled $(In_{50}Bi_{15})Sn_{35}$ solder.

surrounded by the first nucleating In-rich β phase, as is shown in the experimental data in Fig. 10b. The superconducting properties of the β phase are slightly better than those of γ (higher T_c and B_{c2} values at 4.2 K [9]). We note that using more realistic soldering times, the $NbSn_2$ phase will be very much thinner than formed in our extended experiments, but we have demonstrated that the thermodynamics of the system predict it should always be present.

The solidification path for the ternary solder is superimposed on the liquidus projection of In-Sn-Bi system [49] in Fig. 10c. Point '*T*' denotes the initial ternary solder composition which lies in the β phase field but close to the β/γ boundary. At the start of solidification, once again crystals of β nucleate at the S–L interface until the liquid composition reaches the (β + γ) eutectic reaction. With further cooling, the composition of liquid solder moves towards point '*Eu*' where finally the ternary eutectic reaction creates a three-phase mixture of β, γ and $BiIn_2$. The S–L interface in Fig. 9a is thus mostly surrounded by the In-rich β and Sn-rich γ phases, although $BiIn_2$ is found at a few locations. All three of these solder phases are superconducting [9] but the $NbSn_2$ is not, and this emphasises the importance of the Bi addition to the ternary solder which results in the direct contact of superconducting solder phases with the NbTi filaments. This characteristic solder nucleation behaviour at the solid–liquid interface may have an influence on supercurrent flow across these interfaces.

To test the current carrying ability of the ternary soldered joints, NbTi–(In,Bi)Sn joints were fabricated using the matrix replacement method. The transport measurements in Fig. 11a show that joints can pass significant currents, in excess of 200 A, but that these quickly decrease with applied field, demonstrating resistive behaviour above approximately 0.16 T, Fig. 11b. This transport behaviour agrees well with magnetisation measurements on the bulk ternary solder, shown in Fig. 11c, where the critical field is measured as 0.18 T. This suggests that it is the bulk performance of the solder that is the limiting factor for the joint behaviour, not any interfacial reactions.

4. Conclusions

The interactions of the low-temperature superconductor NbTi with InSn based binary and Bi-containing ternary solders at typical soldering temperatures have been examined for the first time. Based on the microstructural characterization and measured superconducting properties, the following observations can be made.

(i) The metallurgical state of the NbTi filament has a strong influence on the microstructure and chemical composition of the (Nb,Ti)Sn_2 phase at the NbTi–InSn interface. The finer grain structure of β-(Nb,Ti) in the more heavily worked multi-filamentary samples may facilitate a higher diffusion flux of Ti, which in turn may encourage the formation of a thicker (Nb,Ti)Sn_2 layer consisting of large scalloped structures with a significantly higher concentration of Ti (Nb:Ti ratio of 0.5:1). By contrast, a thinner (Nb,Ti)Sn_2 phase layer with negligible solubility of Ti (Nb:Ti ratio of 6:1) develops on the larger NbTi monofilaments. For both mono- and multi-filamentary NbTi, the (Nb,Ti)Sn_2 grains grow with random crystallographic orientation.

(ii) The critical temperature (T_c) of the NbTi filaments remains unchanged at ~9.2 K at all the investigated magnetic fields after long soldering operations. The critical current densities, irreversibility fields and pinning force densities decrease for both the mono- and multi-filamentary NbTi samples after soldering due to coarsening of α-Ti precipitates, but by a higher factor for mono-filamentary NbTi than the multi-filamentary sample.

(iii) The soldering operations do not degrade the bulk pinning force more than a simple heat treatment at the same temperature, and in the case of the mono-filamentary sample may even add additional pinning sites to reduce the degradation of superconducting properties.

(iv) We suggest that a reduction in the thermodynamic activity of Sn in Bi-containing alloys leads to the observed lack of any detectable interaction zone, even after long simulated soldering times. When combined with the analysis of the characteristic nucleation behaviour of superconducting phases at the NbTi–(In,Bi)Sn interface, we identify (In,Bi)Sn alloys as a promising choice for lead-free solders to replace PbBi alloys.

CRediT authorship contribution statement

S. Santra: Conceptualization, Data curation, Formal analysis, Investigation, Methodology, Visualization, Writing - review & editing. **T. Davies:** Methodology. **G. Matthews:** Methodology. **J. Liu:** Methodology. **C.R.M. Grovenor:** Conceptualization, Funding acquisition, Visualization, Writing - review & editing. **S.C. Speller:** Conceptualization, Funding acquisition, Visualization, Writing - review & editing.

Declaration of Competing Interest

No potential conflict of interest was reported by the authors.

Acknowledgements

S. Santra would like to acknowledge Royal Society-SERB Newton International Fellowship for funding the research. The authors would like to acknowledge Mr. A. Wheeler for helping with the preparation of quartz sealing, and Dr. Clara Barker and Robert Gresham for their kind assistance in the laboratory. EPSRC grants (EP/K040375/1 and EP/N010868/1) are acknowledged for funding the 'South of England

Analytical Electron Microscope' and the Zeiss Crossbeam FIB/SEM used in this research.

Data availability

The raw/processed data required to reproduce these results cannot be shared at this time as the data also forms part of an ongoing study.

References

[1] G.D. Brittles, T. Mousavi, C.R.M. Grovenor, C. Aksoy, S.C. Speller, Persistent current joints between technological superconductors, Supercond. Sci. Technol. 28 (2015) 093001–093024.
[2] M. Kodama, K. Okamoto, Y. Koga, T. Yamamoto, H. Watanabe, Analysis for formation of current path in the superconducting joint between Nb-Ti wires with the solder matrix replacement method, Supercond. Sci. Technol. 28 (2015), 045019.
[3] S. Liu, X. Jiang, G. Chai, J. Chen, Superconducting joint and persistent current switch for a 7-Tanimal MRI magnet, IEEE Trans. Appl. Supercond. 23 (2013), 4400504.
[4] Official Journal of the European Union, Directive 2014/9/EU2014.
[5] A.K. Gain, L. Zhang, Interfacial microstructure, wettability and material properties of nickel (Ni) nanoparticle doped tin-bismuth-silver (Sn-Bi-Ag) solder on copper (Cu) substrate, J. Mater. Sci. Mater. Electron. 27 (2016) 3982–3994.
[6] A.K. Gain, L. Zhang, Growth mechanism of intermetallic compound and mechanical properties of nickel (Ni) nanoparticle doped low melting temperature tin-bismuth (Sn-Bi) solder, J. Mater. Sci. Mater. Electron. 27 (1) (2016) 781–794.
[7] S. Cheng, C.-M. Huang, M. Pecht, A review of lead-free solders for electronic applications, Microelectron. Reliab. 75 (2017) 77–95.
[8] A.K. Gain, L. Zhang, Microstructure, thermal analysis and damping properties of Ag and Ni nano-particles doped Sn-8Zn-3Bi solder on OSP-Cu substrate, J. Alloys Compd. 617 (2014) 779–786.
[9] T. Mousavi, C. Aksoy, C.R.M. Grovenor, S.C. Speller, Microstructure and superconducting properties of Sn-In and Sn-In-Bi alloys as Pb-free superconducting solders, Supercond. Sci. Technol. 29 (2016), 015012.
[10] Y. Tsui, E. Surrey, D. Hampshire, Soldered joints–an essential component of demountable high temperature superconducting fusion magnets, Supercond. Sci. Technol. 29 (2016), 075005.
[11] D. Gentile, W. Hassenzahl, M. Polak, Temperature measurements using a monofilamentary superconducting NbTi wire in the current sharing state, Cryogenics 20 (1980) 37–40.
[12] S.L. Kruglov, D.I. Shutova, V.I. Shcherbakov, Effect of heat capacity and conductivity of NbTi normal matrix of a composite superconductor on the stability to magnetic flux jumps, Tech. Phys. 62 (2017) 237–242.
[13] R.F. Thornton, Superconducting joint for superconducting wires and coils US Patent 5410288.
[14] C.P. Bean, Magnetization of hard superconductors, Phys. Rev. Lett. 8 (1962) 250–253.
[15] O.Y. Liashenko, S. Lay, F. Hodaj, On the initial stages of phase formation at the solid Cu/liquid Sn-based solder interface, Acta Mater. 117 (2016) 216–227.
[16] C. Toffolon, C. Servant, B. Sundman, Thermodynamic assessment of the Nb-Sn system, J. Phase Equilib. 19 (1998) 479–485.
[17] J. Wang, C. Liu, C. Leinenbach, U.E. Klotz, P.J. Wiggowitzer, J.F. Löffler, Experimental investigation and thermodynamic assessment of the Cu-Sn-Ti ternary system, Calphad 35 (2011) 82–94.
[18] C.-L. Tsao, S.-W. Chen, Interfacial reactions in the liquid diffusion couples of Mg/Ni, Al/Ni and Al/(Ni)-Al_2O_3 systems, J. Mater. Sci. 30 (1995) 5215–5222.
[19] T.H. Chuang, H.M. Wu, M.D. Cheng, S.Y. Chang, S.F. Yen, Mechanisms for interfacial reactions between liquid Sn-3.5 Ag solders and Cu substrates, J. Electron. Mater. 33 (2004) 22–27.
[20] N. Tang, Y.P. Li, S. Kurosu, Y. Koizumi, H. Matsumoto, A. Chiba, Interfacial reactions of solid Co and solid Fe with liquid Al, Corr. Sci. 60 (2012) 32–37.
[21] S.H. Mannan, M.P. Clode, M. Dagher, Study of intermetallic crystal growth between Nb and molten 52In-48Sn solder, J. Electron. Mater. 34 (2005) 125–131.
[22] J.F. Li, S.H. Mannan, M.P. Clode, C. Johnston, A. Crossley, Dissolution and interfacial reaction of Nb in contact with the molten 52In-48Sn solder, Acta Mater. 55 (2007) 5057–5071.
[23] E.N. Popova, V.V. Popov, E.P. Romanov, N.E. Hlebova, A.K. Shikov, Effect of deformation and annealing on texture parameters of composite Cu-Nb wire, Scr. Mater. 51 (2004) 727–731.
[24] V.D. Cojocaru, D. Raducanu, T. Gloriant, D.M. Gordin, I. Cinca, Effects of cold-rolling deformation on texture evolution and mechanical properties of Ti-29Nb-9Ta-10Zr alloy, Mater. Sci. Engg. A 586 (2013) 1–10.
[25] A.R.S. Gautam, J.M. Howe, A method to predict the orientation relationship, interface planes morphology between a crystalline precipitate and matrix: part II – application, Phil. Mag. 93 (2013) 3472–3490.
[26] A. Nordgren, Microstructural characterization of cemented carbides using SEM based automatic image analysis, Ref. Metals and Hard Mater. 10 (1991) 61–81.
[27] F.J.J. van Loo, Multiphase diffusion in binary and ternary solid-state systems, Prog. Solid St. Chem. 20 (1990) 47–99.
[28] T. Laurila, A. Paul, Understanding the growth of interfacial reaction product layers between dissimilar materials, Crit. Rev. Solid State Mater. Sci. 41 (2016) 73–105.
[29] C. Ghosh, A. Paul, A physico-chemical approach in binary solid-state interdiffusion, Acta Mater. 55 (2007) 1927–1939.
[30] S. Santra, A. Paul, Effect of Ti concentration on the growth of Nb_3Sn between solid Nb(Ti) and liquid Sn, J. Electron. Mater. 42 (2013) 2716–2723.
[31] D.C. Palmer, Visualization and analysis of crystal structures using CrystalMaker software, Z. Kristallogr. 230 (2015) 559–572.
[32] S. Roy, S. Prasad, S.V. Divinski, A. Paul, Diffusion pattern in MSi_2 and M_5Si_3 silicides in group VB (M=V, Nb, Ta) and VIB (M=Mo, W) refractory metal-silicon systems, Phil. Mag. 94 (2014) 1508–1528.
[33] H.T.G. Hentzell, K.N. Tu, Interdiffusion in copper-aluminium thin films. II. Analysis of marker motion during sequential compound formation, J. Appl. Phys. 54 (1983) 6929–6937.
[34] P. Kiruthika, A. Paul, Growth of phases and diffusion of components in the W-Pt system, J. Alloy. Compd. 35 (2014) 36–42.
[35] S. Santra, A. Paul, Diffusion of components via different modes during growth of the A15-V_3Ga phase, Phil. Mag. Lett. 94 (2014) 487–494.
[36] Q.Z. Hong, F.M. d'Heurle, The dominant diffusing species and the initial phase formation in Al-Cu, Mg-Cu and Mg-Ni systems, J. Appl. Phys. 72 (1992) 4036–4040.
[37] S. Okuda, M. Suenaga, R.L. Sabatini, Influence of metallurgical factors on superconducting current densities in "bronze-processed" Nb3Sn multifilamentary wires, J. Appl. Phys. 54 (1) (1983) 289–302.
[38] S. Santra, S. Suwas, A. Paul, Effect of Nb orientation and deformation on the growth of Nb_3Sn intermetallic superconductor by bronze technique, Phil. Mag. Lett. 95 (2015) 504–510.
[39] Th. Schneider, P. Turowski, Critical current degradation of a NbTi-multifilament conductor due to heat treatment, IEEE Trans. Magn. 30 (1994) 2391–2394.
[40] C. Scheuerlein, I. Pong, C. Senatore, M.D. Michiel, L. Thilly, A. Gerardin, B. Rehmer, L. Oberli, G. Willering, L. Bottura, Temperature induced degradation of Nb-Ti/Cu composite superconductors, J. Phys. Conf. Ser. 234 (2010) (022031-1-5).
[41] J. Hoellrich, G. Kath, Investigation of the influence of the heat treatment and forming regimes on the critical current and pinning force of NbTi superconductors, Acta Phys. Acad. Sci. Hungar. 53 (1982) 331–336.
[42] D. Dew-Hughes, Flux pinning mechanisms in type II superconductors, Phil. Mag. 30 (1974) 293–305.
[43] C. Meingast, D.C. Larbalestier, Quantitative description of a very high critical current density Nb-Ti superconductor during its final optimization strain. II. Flux-pinning mechanisms, J. Appl. Phys. 66 (1989) 5971–5983.
[44] L. Muzzi, G.D. Marzi, C.F. Zignani, L. Affinito, M. Napolitano, R. Viola, C.O. Domínguez, L. Bottura, S.L. Naour, D. Richter, A.d. Corte, Pinning properties of commercial Nb-Ti wires described by a 2-components model, IEEE Trans. Appld. Supercond. 20 (2010) 1496–1499.
[45] C. Bormio-Nunes, M.J.R. Sandim, L. Ghivelder, Composition gradient as a source of pinning in Nb-Ti and NbTa-Ti superconductors, J. Phys. Condens. Matter 19 (2007) (446204-1-6).
[46] C.F. Zignani, G.D. Marzi, L. Muzzi, J. Somerkoski, Evolution of the pinning force of NbTi filaments as a function of isothermal annealing time, Phys. Procd. 36 (2012) 1406–1411.
[47] J. Someroski, C.F. Zignani, G. De Marzi, L. Muzzi, Metallurgical processes in NbTi filaments as a function of isothermal annealing time, Phys. Procd. 36 (2012) 1516–1521.
[48] J.O. Andersson, T. Helander, L. Höglund, P.F. Shi, B. Sundman, Thermo-Calc and DICTRA, computational tools for materials science, Calphad 26 (2002) 273–312.
[49] V.T. Witusiewicz, U. Hecht, B. Böttger, S. Rex, Thermodynamic re-optimization of the Bi-In-Sn system based on new experimental data, J. Alloy. Compd. 428 (2007) 115–124.
[50] T. Laurila, V. Vuorinen, M. Paulasto-Kröckel, Impurity and alloying effects on interfacial reaction layers in Pb-free soldering, Mater. Sci. Engg. R 68 (2010) 1–38.
[51] T. Laurila, V. Vuorinen, J.K. Kivilahti, Interfacial reactions between lead-free solders and common base materials, Mater. Sci. Engg. R 49 (2005) 1–60.